AIAA SciTech Forum
11–15 & 19–21 January 2021, VIRTUAL EVENT
AIAA Scitech 2021 Forum

10.2514/6.2021-1323

Numerical and Experimental Investigations of Energy Harvesting From Piezoelectric Inverted Flags

Oluwafemi Ojo and Kourosh Shoele
Department of Mechanical Engineering, Florida A&M University - Florida State University College of Engineering, Tallahassee, FL, 32310, USA

Yu-Cheng Wang, Eetu Kohtanen, and Alper Erturk
G.W. Woodruff School of Mechanical Engineering, Georgia Institute of Technology, Atlanta, GA 30332, USA

In this paper, we investigate the piezoelectric energy harvesting performance of inverted flags with different aspect ratio subject to unidirectional flow. Flags with three different aspect ratios were studied both numerically and experimentally to explore the different oscillatory modes of the system and their different energy harvesting capability. Each flag is intrinsically coupled with the piezoelectric patches attached to its surfaces. As the piezo-patches deform with the inverted flag, they generate electrical power which is dependent on the flow, structural and electrical parameters of the problem. Experiments on flags made of spring steel were conducted in a wind tunnel, where the wind speed was swept up through the various vibration modes of the inverted flags. The roles of flow conditions, structural parameters and electric setup on the oscillatory behavior and power capturing efficiency of the inverted flag are assessed and it is discussed that the aspect ratios of the flag can be leveraged to increase the energy harvesting attainable during large amplitude two-sided flapping modes.

I. Nomenclature

m_s	=	Mass per unit area of the flag
ρ	=	Density of the fluid
δ_{ij}	=	Bending and twisting coefficients
σ'_{ij}	=	In-plane compression and tension in the flag
$\mathbf{g}$	=	Gravity
L	=	Length of the flag
U	=	Freestream velocity
κ_b	=	Bending stiffness of the flag
h	=	Flag thickness
M^*	=	Mass number
U^*	=	Reduced velocity
K_b	=	Nondimensional bending stiffness of the flag
μ	=	Dynamic viscosity
$\triangle t$	=	Time step
$\mathbf{f}$	=	Force per unit mass applied on the fluid by the flag
α	=	Inverted flag and piezoelectric patch coupling coefficient
β	=	Resistive coefficient that relates the linear capacitance and the linear conductivity between piezoelectric patches

II. Introduction

The research on renewable energy has been popular for decades, and energy harvesting from environmental wind sources specifically is playing a significant role in the pursuit of sustainable energy generation [1]. Piezoelectric materials can convert internal strain energy to electrical energy [2] and are well suited for energy harvesting in small scale applications. The continuous motion required for energy production by piezoelectric harvesters is easily attainable by taking advantage of aerodynamic instability phenomena, such as aeroelastic flutter [3, 4], vortex-induced vibrations [5, 6], turbulence-induced forces [7, 8] and galloping [9, 10]. Flutter-based harvesters are typically made of

piezoelectric patches bonded to flexible cantilevered structures imitating flags. Extensive studies have been conducted to understand the dynamics and fluttering regimes of flexible plates subjected to axial flow in the regular flag orientation as summarized in the review by Shelley and Zhang [11], where a regular flag orientation is defined as the configuration with a fixed leading edge and a free trailing edge. The inverted flag, on the other hand, is an orientation where the trailing edge is fixed and the leading edge is free to oscillate and can sustain flapping behavior with large deflection amplitudes at relatively low flow speeds [12]. It has been found that the inverted flag configuration is more efficient for energy harvesting than the regular flag configuration at low wind speeds [13]. The inverted flag has three distinct modes of vibration due to its interaction with the flow: a stationary mode, a two-sided flapping mode, and a one-sided flapping mode [14–18]. In addition to these computational approaches, water and wind tunnel experiments have also been conducted which confirm that there are three flapping modes depending on the speed of the incoming flow and the behavior of the shed vortexes behind the flag [15, 16]. The amount of power that can be generated from an inverted flag is directly related to both its frequency and the amplitude of vibration, both of which are tightly coupled with the flow field around the flag. Moreover, the geometrical aspect of the inverted flag, namely its aspect ratio and its alignment with the flow, also affect the oscillatory behavior of the flag and hence its energy harvesting efficiency. To better understand the energy harvesting efficiency of this system, it is crucial to investigate the physical mechanisms which contribute to the dynamic response of the system. In particular, certain design aspects of the inverted flag can influence this fluid-structure-electrical interaction problem, including the aspect ratio of the flag, the bending stiffness of the flag properly scaled with the incoming fluid flow speed and related flow properties, the electrical property of the piezoelectric material, and the unsteadiness of the incoming flow.

In this study, we will explore the flapping dynamics and electrical property of the flag for different aspect ratios and discuss how this can be utilized to enhance its energy harvesting. The robustness of an energy harvester to modifications in the geometry is checked and we explore how to maximize the power generation by the flag. Flow speed ranges in which high amplitude, two-sided flapping occurs are reported for flags with three different aspect ratios, and the influence of aspect ratio on the energy capture is examined.

III. Numerical Formulation

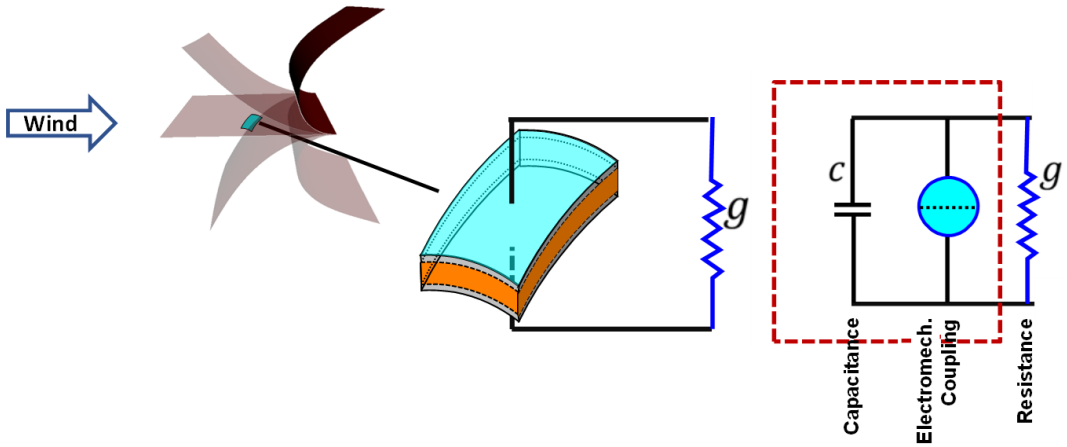

Fig. 1 Inverted piezoelectric flag with incoming fluid flow and the representation of an infinitesimal piezo-patch along with its attached electrical network

A. Governing equations for fluid-structure-electrical coupling of inverted flags

The structural dynamics of the inverted flag without the electrical action is governed by momentum equation written in the flag curvilinear coordinate system ($0 \leq s_1 \leq 1, 0 \leq s_2 \leq 1$) as [13, 19]:

$$m_s \frac{\partial^2 \mathbf{X}}{\partial t^2} = \sum_{i,j=1}^{2} \left[\frac{\partial}{\partial s_i} \left(\sigma'_{ij} \frac{\partial \mathbf{X}}{\partial s_j} \right) - \frac{\partial^2}{\partial s_i \partial s_j} \left(\kappa_b \frac{\partial^2 \mathbf{X}}{\partial s_i \partial s_j} \right) \right] - \mathbf{F} \tag{1}$$

where m_s is the mass of the flag per unit area, ρ is the density of the fluid, κ_b encapsulates the bending and twisting coefficients. Here we assumed that all κ_b coefficient are similar. σ'_{ij} are the in-plane stretching and compressible forces in the flag, and $\mathbf{F}'$ is the force in the Lagrangian frame exerted on the flag by the fluid. The nondimensional form of the equation can be further expressed as:

$$\frac{\partial^2 \mathbf{X}}{\partial t^2} = \sum_{i,j=1}^{2} \left[\frac{\partial}{\partial s_i} \left(\sigma_{ij} \frac{\partial \mathbf{X}}{\partial s_j} \right) - \frac{\partial^2}{\partial s_i \partial s_j} \left(\frac{\kappa_b}{m_s U^2 L} \frac{\partial^2 \mathbf{X}}{\partial s_i \partial s_j} \right) \right] - \frac{\rho L^2}{m_s} \mathbf{F} \tag{2}$$

Following Michelin and Doare [20], we further assume that the surfaces of the flag are covered with infinitesimal piezoelectric patches with discrete sizes much smaller than L, the length of the flag. The electrical output is coupled to the deformation of the flag through mutual interaction between the electric voltage of the patches as a result of the stretch or compression of the patches and charge transfer through the thickness of the flag. The coupling between the electrical voltage of the discrete patch, $V(s,t)$, the charge per unit length, Q, and the deformation of the flag is expressed as,

$$Q(s_1, s_2, t) = cV + \chi \overline{\kappa} \tag{3}$$

$$\frac{\partial \mathrm{Q}}{\partial t} = -gV \tag{4}$$

where c is the linear capacitance of the piezoelectric element, g is the linear conductivity coefficient, $\overline{\kappa}$ is the mean curvature at (s_1, s_2), and χ is the coupling coefficient related to the material properties of the piezoelectric patches.By considering the electrically induced stiffness in the piezoelectric shell equation, the combined electrical-structural equation can be written as,

$$\frac{\partial^2 \mathbf{X}}{\partial t^2} = \sum_{i,j=1}^{2} \left[\frac{\partial}{\partial s_i} \left(\sigma_{ij} \frac{\partial \mathbf{X}}{\partial s_j} \right) - \frac{\partial^2}{\partial s_i \partial s_j} \left(\frac{M^*}{U^{*2}} \frac{\partial^2 \mathbf{X}}{\partial s_i \partial s_j} \right) \right] + \frac{\sqrt{M^*}}{U^*} \sum_{i=1}^{2} \left[\frac{\partial}{\partial s_i} (\alpha \overline{\kappa} V) \right] - M^* \mathbf{F} \tag{5}$$

$$\beta \frac{\partial V}{\partial t} = -V + \frac{\alpha \beta \sqrt{M^*}}{U^*} \frac{\partial}{\partial t} (\overline{\kappa}) \tag{6}$$

The non-dimensional parameters used to characterize the coupled structural-electrical equations can be listed as:

$$M^* = \frac{\rho L^2}{m_s}, \qquad U^* = UL\sqrt{\frac{\rho L}{\kappa_b}}, \qquad \alpha = \frac{\chi}{\sqrt{\kappa_b c}}, \qquad \beta = \frac{c\,U}{g\,L} \tag{7}$$

where L, U, and κ_b are the length, the incoming freestream velocity, and the bending stiffness of the flag, respectively. Other parameters are the mass number, M^* which is the ratio of the inertia of the fluid to the inertia of the structure, and the dimensionless Lagrangian forcing, $\mathbf{F} = \mathbf{F}'/\rho U^2$. The non-dimensional bending stiffness is calculated from the thickness of the plate (h), the Poisson's ratio of the flag (υ) and the Young's modulus (E).The inverted flag has boundary conditions as follows: the fixed boundary is imposed at s_1=1 and the free boundary condition is implemented on on other boundaries.

The Navier-Stokes momentum and continuity equations for incompressible fluids are the governing equations for the fluid flow:

$$\left[\frac{\partial \mathbf{u}}{\partial t} + \nabla \cdot (\mathbf{u}\mathbf{u}) \right] = -\nabla p + \frac{1}{Re} \nabla^2 \mathbf{u} + \mathbf{f} \tag{8}$$

$$\nabla \cdot \mathbf{u} = 0 \tag{9}$$

where $\mathbf{u}$ is the velocity of the fluid flow, p is the dynamic pressure, $Re = \rho UL/\mu$ is the Reynolds number, μ is the dynamic viscosity, and $\mathbf{f}$ is the force per unit mass applied on the fluid by the flag.

B. Numerical implementation

A Crank-Nicolson second-order implicit time advancement scheme was used to solve the fluid, structural, and electric equations:

a) Fluid Equations:

$$\frac{\mathbf{u}^{n+1}-\mathbf{u}^{n}}{\triangle t}+\frac{1}{2}\left(N(\mathbf{u}^{n+1})+N(\mathbf{u}^{n})\right)=-\nabla p^{n+\frac{1}{2}}+\frac{1}{2Re}\nabla^{2}(\mathbf{u}^{n+1}+\mathbf{u}^{n})+\mathbf{f}^{n} \tag{10}$$

$$\nabla\cdot\mathbf{u}^{n+1}=0 \tag{11}$$

b) Structural Equation:

$$\frac{\mathbf{X}^{n+1}-2\mathbf{X}^{n}+\mathbf{X}^{n-1}}{\Delta t^{2}}=\mathbf{K}\mathbf{X}^{n+1}+\frac{\alpha\sqrt{M^{*}}}{U^{*}}\mathbf{H}(\overline{\kappa}^{n+1}V^{n})-\mathbf{F}^{n}+\mathbf{H}\mathbf{T} \tag{12}$$

c) Electric Equation:

$$\frac{V^{n+1}-V^{n}}{\triangle t}=-V^{n+1}+\frac{\alpha\beta\sqrt{M^{*}}}{U}\frac{\overline{\kappa}^{n+1}-\overline{\kappa}^{n}}{\triangle t} \tag{13}$$

where $\mathbf{K}$ is the non-dimensional nonlinear discrete operator which includes the stretching and bending effects, $\mathbf{H}$ is the discrete operator of divergence on the surface of the flag, and $\mathbf{HT}$ includes the boundary condition vector, which consists of the known positions at the fixed boundary. The interaction forces $\mathbf{f}^{n}$ and $\mathbf{F}^{n}$ are related by $\mathbf{f}(\mathbf{x},t)=\int_{\Gamma}\mathbf{F}(s_1,s_2,t)\,\delta\left[\mathbf{x}-\mathbf{X}(s_1,s_2,t)\right]ds_1ds_2$, where Γ is the surface of the flag and δ is the Dirac-delta function. Here, $N(\mathbf{u})$ operator denotes the nonlinear convective term and k is sub-iteration used at each time step for solving the flow equations.

C. Simulation setup

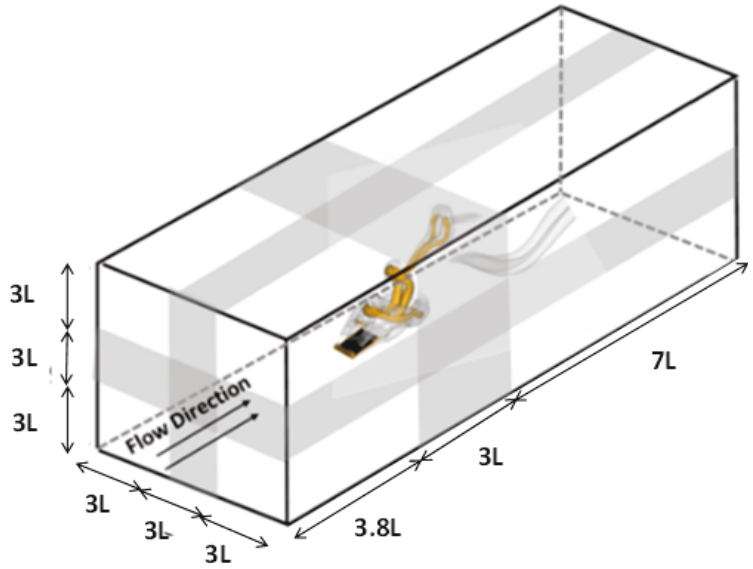

Fig. 2 The schematic figure of the fluid domain and the inverted piezoelectric flag

Figure 2 shows the rectangular computational domain surrounding the inverted flag and a sample vortex structure around the flag. The size of the computational domain was fixed at $-4L \le x \le 9.8L$, $-4.5L \le y \le 4.5L$, $-4.5 \le z \le 4.5L$, and the fluid grid size is selected as 252×128×128 following the grid convergence study. The grid points surrounding the flag are more refined with $\Delta x = \Delta y = 0.025L$. The Reynolds number used for the current simulations is set at 400, and the mass ratio (M^{*}) is 0.1. A uniform velocity was assumed at the inlet and side boundaries and a convective outflow boundary condition was assumed at the outlet. A zero normal gradient boundary condition was used for pressure on all boundaries. Simulations were run for flags with constant length L and width to length aspect ratios ranging from slender to wide flags. The computational parameters have been checked to ensure their adequacy for the current study.

D. Experimental setup

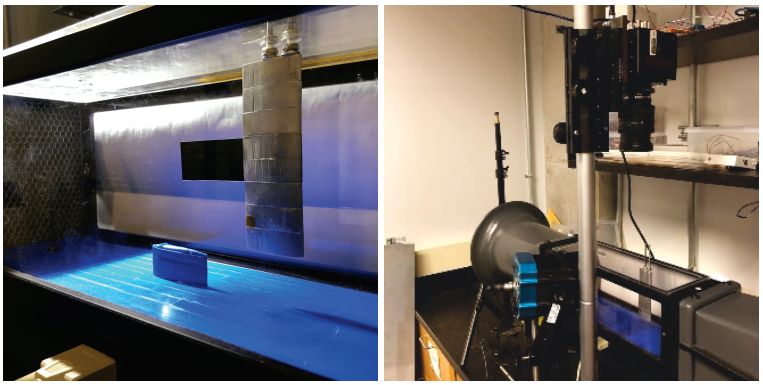

Fig. 3 Experimental setup for the inverted flags where (left) an inverted flag was clamped in an airfoil-shaped support section and pointed into the flow, and (right) a high speed camera was placed above the test section of the wind tunnel to capture a top view of the flag.

The experiments on inverted flags with AR = 1 were conducted in a wind tunnel under increasing wind speeds as shown in Figure 3. The inverted flag sample was clamped by eight of half-inch airfoil-shaped(NACA 0010) aluminum sections which was cut by wire electrical discharge machining from a raw aluminum 6061 sheet. A high-speed camera was used to capture the top view of the flapping motion of the inverted flag within the test section as shown in Figure 3. Videos were then analyzed with MATLAB to obtain the dynamic response of the inverted flags. The experiment on the inverted flag started from zero wind speed. Different vibration modes were observed as the wind speed was incremented by 0.447 m/s at a time. The peak-to-peak displacement was then extracted from these videos as a function of the wind speed for each sample.

IV. Results

A. Flapping Dynamics of an Inverted Flag

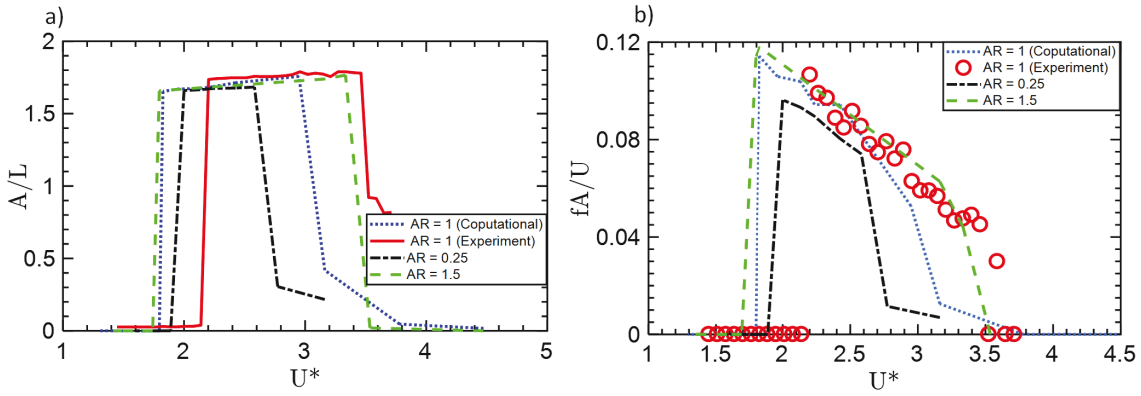

Fig. 4 (a) Peak-to-peak displacement amplitude of the flag against U* for AR= 0.25 (black), 1-experimental (red) , computational (blue),and 1.5 (green) b) strouhal number of the flag against nondimensional freestream velocity (U*) for AR= 0.25 (black), 1-experimental (red) , computational (blue),and 1.5 (green)

Initially, we assumed that there is no electrical coupling. Three distinct vibration modes were observed experimentally and numerically using the inverted flag model for a length to width ratio of 1. For low non-dimensional speed values of $U^* \leq 1.8$ and $U^* \leq 2.1$, corresponding to numerical and experimental results, it was observed that the inverted flag remains motionless (Figure 4a). This is referred to as the stationary mode. The second vibration mode, is a

two-sided, self-sustained flapping mode. The flag experiences its highest amplitude at this stage and oscillate in its most energetic mode. The amplitude also increases as U^* increases within this region and is observed both numerically and experimentally at intermediate velocity values of $1.82 \leq U^* \leq 3$, and $2.3 \leq U^* \leq 3.5$ respectively. The last vibration mode is a one-sided flapping or deflected mode. This mode is observed for higher velocity values of $U^* > 3$ numerically and $U^* > 3.5$ experimentally.

An increase in AR results in a larger flapping region while reduction in AR leads to a smaller flapping region as plotted in Figure 4a. For a slender flag, AR = 0.25, the critical flapping velocity shifts to the right at $U^* = 1.9$ and experiences two-sided flapping at $1.92 \leq U^* \leq 2.65$ while at $U^* > 2.7$ the flag remains deflected. For wider flags, at AR = 1.5, the critical flapping velocity shifts slightly to the left, where the flag exhibits a stationary mode at $U^* \leq 1.7$, flapping mode at $1.71 \leq U^* \leq 3.5$, and deflected mode at $U^* > 3.5$. An increase in flag aspect ratio leads to more efficient two-sided flapping response over a wider range of non-dimensional velocity.

For AR = 1, zero frequency is observed at low U^* both experimentally and numerically as shown in Figure 4b. At the flapping region, the flag experiences its highest Strouhal number(defined as $St = fA/L$ with f and A being the frequency and amplitude of the vibration) at the onset of flapping both numerically and experimentally at $U^* = 1.82$, and $U^* = 2.3$, respectively. As U^* increases through the flapping region, the St continues to decrease even though the amplitude remains constant. This reduction is due to a delayed symmetric motion at the tip of the flag when it reaches the maximum amplitude at high U^*. At higher U^*, the flag takes its deflected stationary mode and St returns back to zero.

For slender (AR = 0.25) and wide (AR = 1.5) flags as shown in Figure 4b, the flag experiences the same frequency trend as the flag with AR = 1. When AR = 0.25, the flag shows the lowest St among the tested cases. This is because the width of the flag is narrow and the leading-edge vortex (LEV) which contributes to the flapping dynamics of the flag is smaller. As AR increases, the LEV starts to play a more significant role in its flapping dynamics, thereby causing the flag to flap at a higher frequency. An increase in St also occurs at AR = 1.5, in which the LEV becomes more stable and attains its shape over most of the flag width.

B. Effect of Vortical Structures on Flapping Dynamics

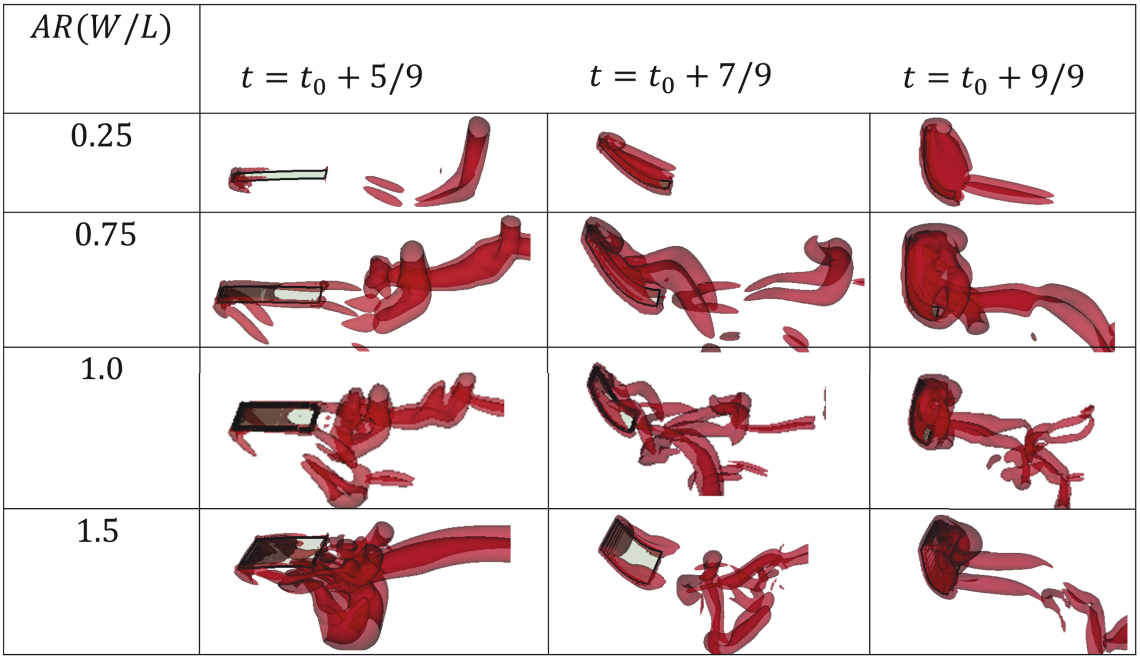

Fig. 5 Q-criterion vortical structure around the flag for AR = 0.25, 0,75,1.0 and 1.5.

The flapping of an inverted flag is a results of a vortex-induced vibration and to better understand the relation between the flapping dynamics and flow field, we plot the vortical structures using the Q-criterion (Q). Here, we show the 3D vortices of the flag at an iso-surface of Q = 2. In can be observed that in all cases, the leading-edge vortex

(LEV) and side edge vortices (SEVs) interact with the flag to allows periodical flapping motion. At the initiation of flapping motion, a vortical core develops at the leading edge, quickly followed by the SEVs. When the flag reaches its maximum deflected position, the combination of vortices pushes it in the opposite direction, enabling the symmetric oscillation. In Figure 5, for slender flags, i.e. AR = 0.25, at t = t_0 + 5/9, a small strip of LEV can be seen when the flag is parallel to the flow. As the flag deforms further, at t = t_0 + 9/9, the side vortices start to push the flag upwards until it reaches maximum deflection. LEV plays a minimal role in this AR due to the small width to length ratio of the flag, making the flapping dynamics mainly a function of SEVs. As AR increases, AR = 0.75 - 1.0, both LEV and SEVs have similar impacts on the flapping dynamics of the flag. At t = t_0 + 7/9, a strong vortex is formed before the flag reaches its maximum deformation. Here, LEV becomes more dominant and connects SEVs from both edges to form a vortex ring in the wake as can be seen in Figure 5. For wider flags, AR = 1.5 - 2.0, LEV is the sole dominant vortex feature and SEVs play much smaller role through the flapping cycle. At t = t_0 + 7/9, the vortex behind the flag seen in the previous AR breaks up while the LEV becomes more prominent due to the increase in width of the flag. Flags with higher AR experience the stronger vortices, since the LEV does not substantially deflect by the SEVs. Stronger LEV here keeps the flag flapping over a larger range of U^* compared with other ARs as seen in Figure 4. Here we can see that AR = 1.5 has the lowest critical flapping velocity.

C. Piezoelectric Energy Harvesting

Reynolds Number	400
U^*	2.09
Mass Ratio	0.1
α	0.1 - 0.5
β	0.1 - 10
AR	0.25 - 1.5

Table 1 Piezoelectric energy harvesting parameters.

In this section, we assume that the flag is made up of piezoelectric patches and we examine how the aspect ratio affects the energy harvesting performance of the system. As mentioned in section III, the surfaces of the flag is covered with infinitesimal piezoelectric patches with discrete lengths much smaller than L. The piezoelectric energy (P_p) is calculated from normalizing the harvested power is calculated from normalizing the harvested power (P= $\frac{1}{T\beta M^*}\int_0^T \int_0^1 V^2\, ds$) with the kinetic energy flux of the fluid around the flag ($\rho U^3 L$) [20].From the results presented above in section IV.B, we select ARs = 0.25, 0.75, and 1.5, and fixed Re = 400 and U^* = 2.09. This values are chosen as representative cases that ensures the flag undergoes a sustained two-sided flapping motion for all AR. α, which quantifies the electromechanical coupling strength of piezoelectric patches, takes a value between 0.1 - 0.5. Also β, which is a resistive coefficient that relates the linear capacitance and the linear conductivity between piezoelectric patches changes between 0.1 – 10. Table 1 summarizes the parameters used in this section.

1. Low electromechanical coupling ($\alpha = 0.1$)

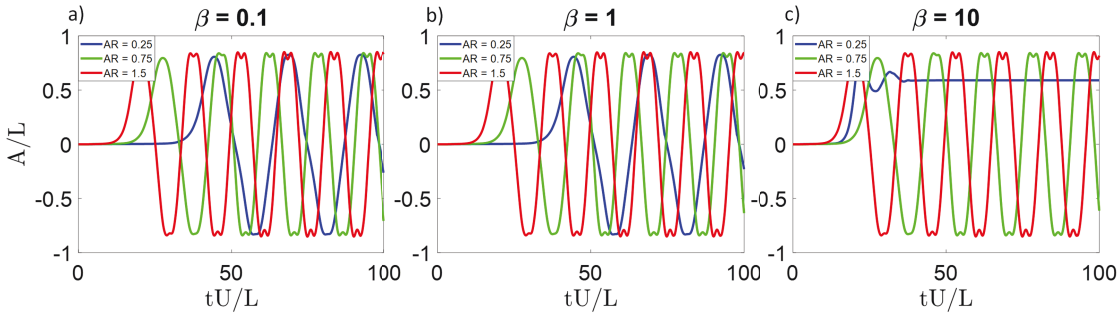

Fig. 6 Flapping amplitude of the flag during energy harvesting when α = 0.1 for AR = 0.25 (blue), 0.75 (green), 1.5 (red) a) β = 1, b) β = 0.1 c) β = 10.

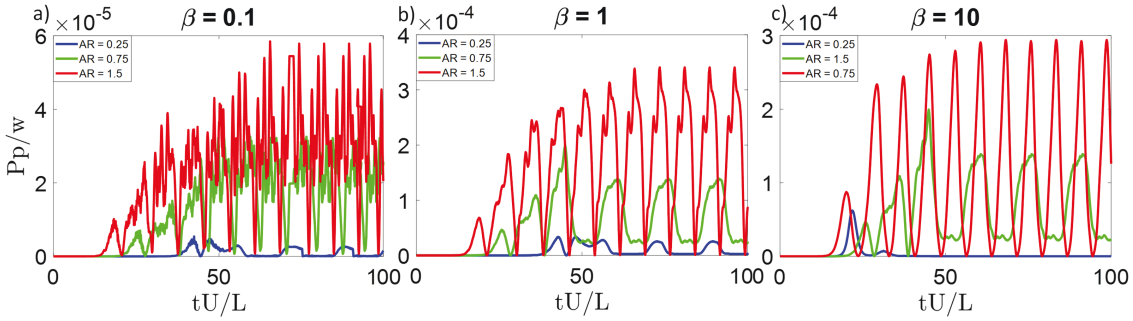

Fig. 7 Piezoelectric energy harvested in the flag for AR = 0.25 (blue), 0.75 (green), 1.5 (red) for a) β = 1, b) β = 0.1 c) c) β = 10.

When the electromechanical coupling coefficient is low (here α = 0.1), the piezoelectric patch is loosely coupled to the inverted flag and there is a limited feedback from the electrical charges on the flapping modes of the flag. A resistive coefficient of 0.1 - 10 is simulated for AR= 0.25 – 1.5. For β = 0.1, the flapping amplitude is similar for all AR's as shown in Figure 6a but the piezoelectric energy increases with an increase of AR (Figure 7a). As the resistive coefficient increases to β = 1, similar trend can be found. Also, an overall increase in P_p is noticed at this resistive coefficient when compared with β = 0.1. When the resistive coefficient of the piezoelectric material increases further to β = 10, the low aspect ratio flag with AR = 0.25 does not flap but undergoes bifurcation and takes a deflected stationary shape. This is not seen for higher ARs. Here, instead flags are able to accommodate such high β and continue their two-sided flapping motions. The P_p at AR = 0.25 is zero while for higher width to length ratios, P_p increases with AR. At β = 10, the overall P_p reduces slightly because the mismatch between the timescales of mechanical and electrical subdomains. Still the harvested energy is higher than β = 0.1.

2. Medium electromechanical coupling ($\alpha = 0.3$)

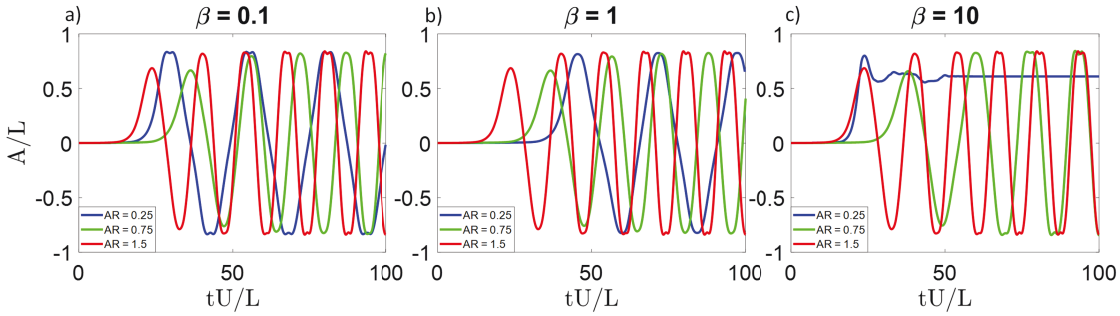

Fig. 8 Flapping amplitude of the flag during energy harvesting when α = 0.3 for AR = 0.25 (blue), 0.75 (green), 1.5 (red) a) β = 1, b) β = 0.1 c) β = 10.

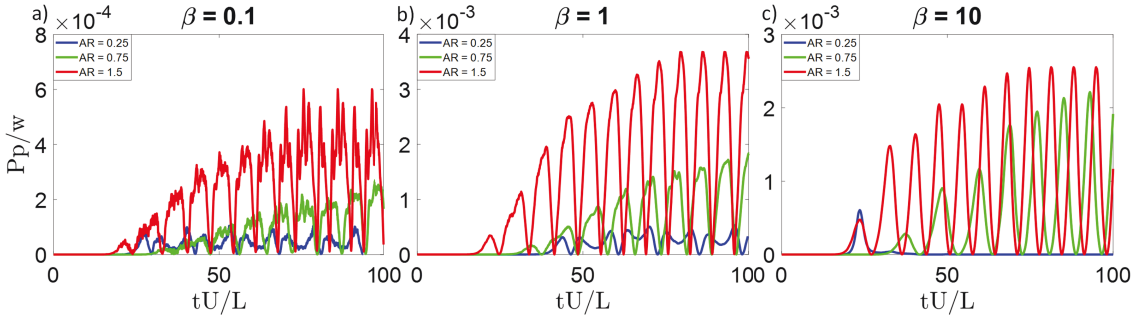

Fig. 9 Piezoelectric energy harvested in the flag when α = 0.3 for AR = 0.25 (blue), 0.75 (green), 1.5 (red) a) β = 1, b) β = 0.1 c) β = 10.

When the piezoelectric material has a higher coupling coefficient, here $\alpha = 0.3$ (α is a characteristic of the material's electric and mechanical properties and could be of the order 0.3 for typical piezoelectric materials such as PZT), almost the same trend occurs as when $\alpha = 0.1$ and the response of the flag only marginally modifies. When $\beta = 0.1$, the flapping amplitude is equal for all AR's as seen in Figure 8a but the delay in the flapping motion at maximum deflection seen previously for $\alpha = 0.1$ is damped out very fast here. Also, the P_p increases with an increase in AR as illustrated in Figure 9a. As the resistive coefficient increases to $\beta = 1$, the same trend is noticed. The flapping amplitude remains insensitive to aspect ratio and β while the piezoelectric energy harvested (P_p) increases with AR. The flag also experiences a deflected mode when AR = 0.25 and $\beta = 10$.

3. High electromechanical coupling ($\alpha = 0.5$)

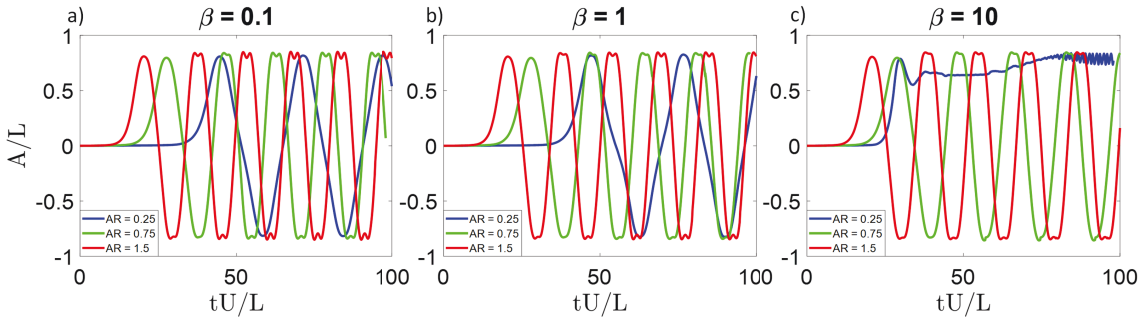

Fig. 10 Flapping amplitude of the flag during energy harvesting when α = 0.5 for AR = 0.25 (blue), 0.75 (green), 1.5 (red) a) β = 1, b) β = 0.1c) β = 10.

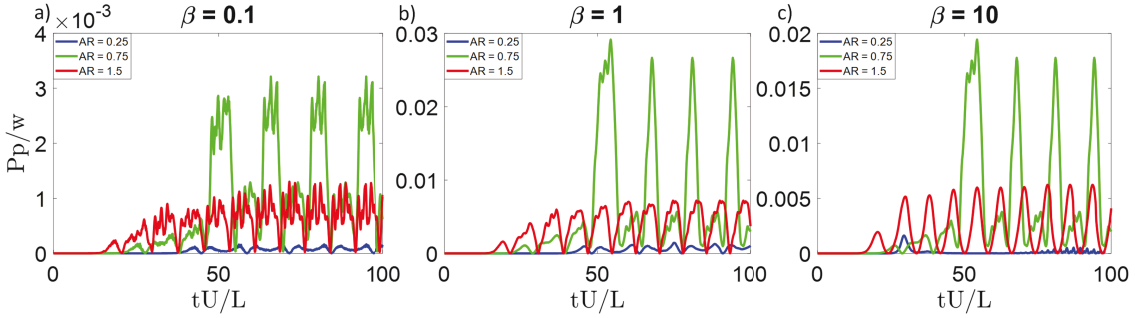

Fig. 11 Piezoelectric energy harvested in the flag when α = 0.5 for AR = 0.25 (blue), 0.75 (green), 1.5 (red) a) β = 1, b) β = 0.1 c) β = 10.

For α = 0.5, the piezoelectric patch is even more coupled with the inverted flag. For all β values, the flapping amplitude continues to be similar among all ARs, but the delay at the maximum deflection, is observed again as seen in Figure 10a-c. The major changes for high electromechanical coupling coefficient is related to tightly coupled time responses of electrical and mechanical systems and potential asymmetric changes in the deflection shape of the flag during its upward and downward motions. For all β values tested here, when AR = 0.25, P_p is the lowest while the highest P_p is observed at AR = 0.75 (Figure 11a-c). The noticeable increase of the harvested power by AR = 0.75 is linked to constructive interaction between flow, structure and electrical system in this case, which suggests that by finding an optimal interaction between these three phases, it would be possible to substantially increase the energy harvesting efficiency of piezoelectric flags. As the resistive coefficient increases to β = 1, the same trend is noticed but the overall P_p increases. When β = 10, P_p reduces slightly compared to what has been observed in the previous cases.

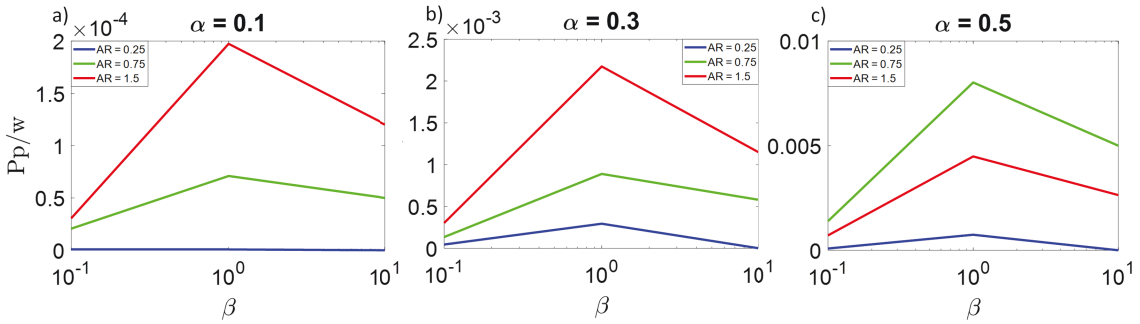

Fig. 12 Piezoelectric energy harvested in the flag when α = 0.1 - 0.5 for AR = 0.25 (blue), 0.75 (green), 1.5 (red) a) β = 1, b) β = 0.1 c) β = 10.

When we compare the energy harvested for all α, β and ARs, we observed that the overall energy harvested increases as the electromechanical coupling of piezoelectric patches increase, and there is limited feedback from electrical system to the oscillating flag or equivalently the stiffening of the flag is primarily set by its material properties and not the electrical actions. Also, when α = 0.1 - 0.3, P_p increases as AR increases but when α = 0.5, the highest P_p is observed at AR = 0.75. We also observed that the highest P_p is captured when the resistive coefficient is 1 related to perfect achievable tuning of the fluid-solid and electric time scales for all α and AR. Slender flags are consistently found to have the lowest overall P_p due to their small flapping frequencies as shown in Figure 4b.

V. Conclusion

Three modes of deformation were observed for different aspect ratios of an inverted flag in a uniform flow both experimentally and numerically: the stationary mode, the flapping mode and the deflected mode. These modes are strongly dependent on the non-dimensional velocity of the flag. It was observed that the flapping frequency of the flag increases as the flag aspect ratio increases and the critical flapping velocity also increase with an increase of AR due to an increase in the leading-edge vortex strength. For the piezoelectric flag, the overall harvested energy increases for higher coupling coefficient between the inverted flag and the piezoelectric patches. AR = 0.75 was identified to be the most efficient aspect ratio compared to AR = 0.25 and 1.5 at high α while AR = 1.5 is more efficient for lower α cases. As the resistive coefficient of the piezoelectric material approach 1, more electrical energy is harvested and the level of electrical energy decreases with an increase or decrease of β coefficient. It is consistently observed that β = 1 is the most efficient resistive coefficient over which there is the best tuning between electrical and mechanical timescales. We are currently exploring the underlying physics of the peculiar response mode of AR = 0.75 and α = 0.5 to better understand what mechanisms result in an asymmetric electrical output and how the higher electromechanical coupling coefficient could cause constructive changes in the flow field around the flag.

References

[1] Evans, A., Strezov, V., and Evans, T. J., "Assessment of sustainability indicators for renewable energy technologies," *Renewable and sustainable energy reviews*, Vol. 13, No. 5, 2009, pp. 1082–1088.

[2] Anton, S. R., and Sodano, H. A., "A review of power harvesting using piezoelectric materials (2003–2006)," *Smart materials and Structures*, Vol. 16, No. 3, 2007, p. R1.

[3] Bryant, M., Wolff, E., and Garcia, E., "Aeroelastic flutter energy harvester design: the sensitivity of the driving instability to system parameters," *Smart Materials and Structures*, Vol. 20, No. 12, 2011, p. 125017.

[4] Dunnmon, J., Stanton, S., Mann, B., and Dowell, E., "Power extraction from aeroelastic limit cycle oscillations," *Journal of Fluids and Structures*, Vol. 27, No. 8, 2011, pp. 1182–1198.

[5] Bryant, M., Mahtani, R. L., and Garcia, E., "Wake synergies enhance performance in aeroelastic vibration energy harvesting," *Journal of Intelligent Material Systems and Structures*, Vol. 23, No. 10, 2012, pp. 1131–1141.

[6] Shafer, M. W., Bryant, M., and Garcia, E., "Designing maximum power output into piezoelectric energy harvesters," *Smart Materials and Structures*, Vol. 21, No. 8, 2012, p. 085008.

[7] Akaydin, H. D., Elvin, N., and Andreopoulos, Y., "Energy harvesting from highly unsteady fluid flows using piezoelectric materials," *Journal of Intelligent Material Systems and Structures*, Vol. 21, No. 13, 2010, pp. 1263–1278.

[8] Hobeck, J., and Inman, D., "A distributed parameter electromechanical and statistical model for energy harvesting from turbulence-induced vibration," *Smart Materials and Structures*, Vol. 23, No. 11, 2014, p. 115003.

[9] Jung, H.-J., and Lee, S.-W., "The experimental validation of a new energy harvesting system based on the wake galloping phenomenon," *Smart Materials and Structures*, Vol. 20, No. 5, 2011, p. 055022.

[10] Akaydın, H., Elvin, N., and Andreopoulos, Y., "Wake of a cylinder: a paradigm for energy harvesting with piezoelectric materials," *Experiments in Fluids*, Vol. 49, No. 1, 2010, pp. 291–304.

[11] Shelley, M. J., and Zhang, J., "Flapping and bending bodies interacting with fluid flows," *Annual Review of Fluid Mechanics*, Vol. 43, 2011, pp. 449–465.

[12] Huang, W.-X., Shin, S. J., and Sung, H. J., "Simulation of flexible filaments in a uniform flow by the immersed boundary method," *Journal of Computational Physics*, Vol. 226, No. 2, 2007, pp. 2206–2228.

[13] Shoele, K., and Mittal, R., "Energy harvesting by flow-induced flutter in a simple model of an inverted piezoelectric flag," *Journal of Fluid Mechanics*, Vol. 790, 2016, pp. 582–606.

[14] Ojo, O., Tan, D., Wang, Y.-C., Shoele, K., and Erturk, A., "Aspect ratio effects in wind energy harvesting using piezoelectric inverted flags," *Active and Passive Smart Structures and Integrated Systems XII*, Vol. 10967, International Society for Optics and Photonics, 2019, p. 109670Q.

[15] Sader, J. E., Cossé, J., Kim, D., Fan, B., and Gharib, M., "Large-amplitude flapping of an inverted flag in a uniform steady flow–a vortex-induced vibration," *Journal of Fluid Mechanics*, Vol. 793, 2016, pp. 524–555.

[16] Kim, D., Cossé, J., Cerdeira, C. H., and Gharib, M., "Flapping dynamics of an inverted flag," *Journal of Fluid Mechanics*, Vol. 736, 2013.

[17] Park, J. W., Ryu, J., and Sung, H. J., "Effects of the shape of an inverted flag on its flapping dynamics," *Physics of Fluids*, Vol. 31, No. 2, 2019, p. 021904.

[18] Gurugubelli, P., and Jaiman, R., "Self-induced flapping dynamics of a flexible inverted foil in a uniform flow," *Journal of Fluid Mechanics*, Vol. 781, 2015, pp. 657–694.

[19] Huang, W.-X., and Sung, H. J., "Three-dimensional simulation of a flapping flag in a uniform flow," *Journal of Fluid Mechanics*, Vol. 653, 2010, pp. 301–336.

[20] Michelin, S., and Doaré, O., "Energy harvesting efficiency of piezoelectric flags in axial flows," *Journal of Fluid Mechanics*, Vol. 714, 2013, pp. 489–504.